

# Numerical and Experimental Investigation of Hydrodynamic Characteristics of Deformable Hydrofoils

Antoine Ducoin,\* François Deniset,\* Jacques André Astolfi,\* and Jean-François Sigrist†

\*Institut de Recherche de l'Ecole Navale (IRENav), BP 600, 29240 Brest Armées, France

†Service Scientifique et Technique, DCNS Propulsion, 44620 La Montagne, France

---

The present paper is concerned with the numerical and experimental investigation of the hydroelastic behavior of a deformable hydrofoil in a uniform flow. The study is developed within the general framework of marine structure design and sizing. An experimental setup is developed in the IRENav hydrodynamic tunnel in which a cambered rectangular hydrofoil is mounted. An image-processing device enables the visualization of the foil displacement. As for the numerical part, the structure problem is solved with the finite element method, while the fluid problem is solved with the finite volume method using two distinct numerical codes that are coupled through an iterative algorithm based on the exchange of the boundary conditions at the fluid-structure interface. Results obtained from the coupled fluid-structure computations including deformation and hydrodynamic coefficients are presented. The influence of the fluid-structure coupling is evaluated through comparisons with “noncoupled” simulations. The numerical simulations are in very good agreement with the experimental results and highlight the importance of the fluid-structure coupling consideration. Particular attention is paid to the pressure distribution modification on the hydrofoil as a result of deformations that can lead to an advance of the cavitation inception, which is of paramount importance for naval applications.

**Keywords:** hydrodynamics (general); hydrofoil

---

## 1. Introduction

THERE has been a growing interest for coupled fluid structure problems in the past decades in many engineering applications. Coupled fluid-structure problems can be categorized in two main areas depending whether the fluid is flowing or not. A first class of coupled problems is concerned with the elastic behavior of a structure in contact with a compressible inviscid fluid that vibrates about a stagnant state (Axisa 2006); a second class of problems involves a deformable structure coupled with a fluid with nonstationary flow (Païdoussis 1998, Païdoussis 2003). In the former category of problems, the structure and the fluid are supposed to have linear behavior and are then described within the framework of elastic vibrations. As a consequence, numerical calculations of the coupled problem can then be performed in the

frequency domain. Many numerical methods, mostly finite element and boundary element methods (Mackerle 1999), have been proposed to take coupling effects into account in various engineering domains, for instance in the nuclear power industry (Gibert 1986) and the aerospace industry (Morand & Ohayon 1995). Such methods have been firmly validated from the theoretical, numerical, and even experimental viewpoints, and their application to industrial problems for design purposes is still an actual concern, in particular in the shipbuilding industry for propellers for instance (Young 2007). In the latter category of problems, the numerical simulation of the coupled systems requires the calculation of the structure displacement field and the fluid pressure and velocity fields in the space-time domain, for which solving nonlinear equations for the fluid and/or structure domains is often needed (Schäfer & Teschauer 2001). Such methods have been initially investigated for aeroelasticity problems (Piperno et al. 1995, Piperno 1997, Piperno & Farhat 2001) and are currently implemented into commercial codes, thus

---

Manuscript received at SNAME headquarters March 27, 2007; revised manuscript received December 31, 2008.

contributing to development of coupled fluid structure studies in many industrial domains (Sigrist & Abouri 2006).

As far as aerodynamic applications are concerned, many studies have highlighted that structural deformation of an elastic solid under static or dynamic loads may be of primary importance in the evaluation of aerodynamic performances (Bhardwaj 1997, Send 1999, Lund et al. 2001, Engel & Griebel 2004, Patil & Hodges 2004, Eller & Heinze 2005). In particular, Bhardwaj (1997) developed a numerical coupling procedure that combined a variety of computational fluid dynamic (CFD) and computational structural dynamic (CSD) codes, applied to wing geometries, and he stressed the importance of the computation initialization from a CFD steady-state solution on the rigid structure on prediction of the wing static deformation. Send (1999) and Patil and Hodges (2004) highlighted a correlation between wing deformation (mainly twist caused by vertical displacement) and variation of hydrodynamic coefficients as lift or wall pressure coefficients.

In the context of hydroelasticity, Kuo and Vorus (1985) developed a coupled procedure solved in the frequency domain for blade stress analysis and noncavitating propellers. They used a potential-based method for the fluid and a finite-element method (FEM) for the structure. In a recent publication, Young (2007) presents an approach applied to a cavitating propeller that takes into account the modification of fluid pressure field induced by the blade displacement. Nonlinear hydroelastic behavior of propellers has been also investigated by Lin and Lin (1996) using lifting surface theory and Young et al. (2006) for composite propellers. The present work is then conducted in the context of hydroelasticity applied to lifting bodies, with possible industrial applications in shipbuilding for the study of propeller hydrodynamic performances, or rudders and ship stabilizer vibration prediction and control. The study presents a numerical and experimental investigation of the hydroelastic behavior of a deformable hydrofoil in a uniform flow, with the view to determine the influence of fluid structure coupling on the hydrofoil hydrodynamic loading and deformation. It is based on both numerical and experimental approaches, carried out for the same geometry with similar boundary conditions. Moreover, the computations are performed with a CFD/CSD coupled methodology in which most of the CFD com-

putations are conducted by solving the Navier-Stokes equations for a viscous fluid. This is a rather new approach as far as hydroelasticity problems are concerned. In many related publications, the fluid viscosity is usually neglected or accounted for through additional terms, mostly for computational cost reasons (Young 2007, Lin & Lin 1996). This latter aspect is discussed in the paper by comparing viscous and nonviscous (Euler) computations.

Mathematical modeling and numerical resolution of coupled fluid-structure problem are first exposed. The numerical method lies on CFD and CSD codes coupling using an iterative procedure. This enables the calculation of the uniform incompressible flow around the hydrofoil at different angles of incidence and the resulting hydrofoil deformation. The experimental setup is then detailed. The study is carried out on a cambered rectangular hydrofoil, which is mounted in the hydrodynamic tunnel at Institut de Recherche de l'Ecole Navale (IRENav), and displacement of the free tip section of the hydrofoil is determined by image processing. Comparisons of experimental and numerical results are then proposed and allow us to validate the numerical procedure and to conclude on the influence of the fluid structure coupling on the hydrofoil hydrodynamic characteristics. Particular attention is paid to the pressure distribution modification on the hydrofoil resulting from deformations that can lead to an advance of the cavitation inception; this aspect is of paramount importance for naval applications (Hauville et al. 1999, Deniset et al. 2002, Leroux et al. 2005).

## 2. Fluid-structure interaction modeling and numerical resolution

### 2.1. Fluid structure coupled equations

Figure 1 sketches a typical fluid-structure coupled problem: let  $\Omega_S$  be the structure domain of boundary  $\partial\Omega_S = \partial\Omega_{S_0} \cup \partial\Omega_{S_\sigma} \cup \Gamma$ , where  $\partial\Omega_{S_0}$  is the boundary part with imposed displacement,  $\partial\Omega_{S_\sigma}$  the boundary part with imposed forces, and  $\Gamma$  the interface with the fluid domain; let  $\Omega_F$  be the fluid domain of boundary  $\partial\Omega_F = \partial\Omega_{F_0} \cup \partial\Omega_{F_\pi} \cup \Gamma$ , where  $\partial\Omega_{F_0}$  is the boundary part with imposed pressure,  $\partial\Omega_{F_\pi}$  the boundary part with imposed velocity,

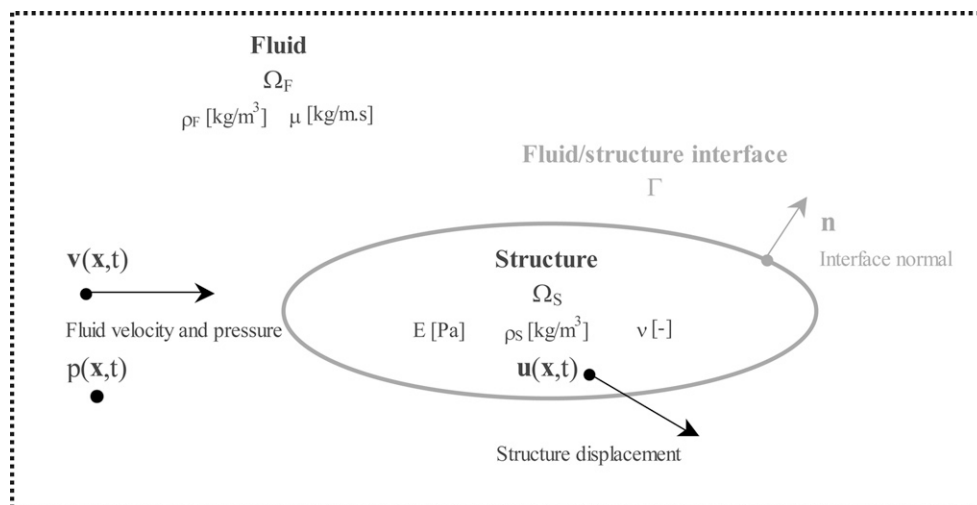


Fig. 1 Elastic structure immersed in a flowing fluid

and  $\Gamma$  the interface with the structure domain. The structure behavior is described in the framework of linear elasticity, using a displacement formulation:

$$\rho_s \frac{\partial^2 u_i}{\partial t^2} - \frac{\partial \sigma_{ij}(\mathbf{u})}{\partial x_j} = 0 \text{ in } \Omega_s \quad (1)$$

$$u_i = 0 \text{ on } \partial\Omega_{s0} \quad (2)$$

$$\sigma_{ij}(\mathbf{u}) \cdot n_j = 0 \text{ on } \partial\Omega_{s\sigma} \quad (3)$$

where  $\mathbf{u} = (u_i)$  and  $\boldsymbol{\sigma}(\mathbf{u}) = \sigma_{ij}(\mathbf{u})$  denote the structure displacement and stress fields respectively,  $\rho_s$  stands for the structure density, and  $\mathbf{n} = (n_i)$  is the outward normal on the structure boundary  $\partial\Omega_s$ .

The fluid flow is described with the mass and momentum conservation equations that read for an incompressible and viscous fluid:

$$\frac{\partial v_j}{\partial x_j} = 0 \text{ in } \Omega_F \quad (4)$$

$$\frac{\partial(\rho_F v_i)}{\partial t} + \frac{\partial(\rho_F v_i v_j)}{\partial x_j} = -\frac{\partial p}{\partial x_i} + \mu \frac{\partial^2 v_i}{\partial x_j^2} \text{ in } \Omega_F \quad (5)$$

$$p = P_o \text{ on } \partial\Omega_{F0} \quad (6)$$

$$v_i = V_o \text{ on } \partial\Omega_{F\pi} \quad (7)$$

where  $\rho_F$  and  $\mu$  are the fluid density and the dynamic viscosity,  $p$  and  $v = (v_i)$  are the fluid pressure and velocity fields.  $P_o$  and  $V_o$  are the imposed fluid pressure and velocity on boundaries  $\partial\Omega_{F0}$  and  $\partial\Omega_{F\pi}$ . For an inviscid fluid, the viscosity term vanishes and the flow is governed by the Euler equations in  $\Omega_F$ .

Coupling conditions are expressed as follows:

- On the one hand, the structure is subjected to imposed local fluid forces that are derived from the fluid stress tensor; boundary condition of the structure problem on  $\Gamma$  reads:

$$\sigma_{ij}(\mathbf{u}) \cdot n_j = \left[ -p\delta_{ij} + \mu \left( \frac{\partial v_i}{\partial x_j} + \frac{\partial v_j}{\partial x_i} \right) \right] \cdot n_j \quad (8)$$

- On the other hand, the fluid is subjected to local imposed displacement as a result of the structure motions; boundary condition of the fluid problem on  $\Gamma$  reads:

$$v_i = \frac{\partial u_i}{\partial t} \quad (9)$$

The main objective of the present study is to perform coupled CFD/CSD simulations of the flow-structure interaction problem, under the assumption of a viscous fluid flow. However, for the sake of comparison, Euler computation will be performed with the same CFD code. In this context, coupling conditions for inviscid flow given by equations (8) and (9) will read

$$\sigma_{ij}(\mathbf{u}) \cdot n_j = pn_i$$

and

$$v_i \cdot n_i = \frac{\partial u_i}{\partial t} \cdot n_i$$

## 2.2. Numerical resolution of the fluid-structure problem

The numerical resolution of the coupled fluid-structure problem is carried out using a code coupling methodology. The structure

problem is solved with the finite element technique (Zienkiewicz & Taylor 1989), using the CSD code ANSYS. The variational formulation of the structure problem is the starting point of the method. Multiplying equation (1) by any virtual displacement field  $\delta\mathbf{u}$ , integrating by parts, taking into account boundary conditions and using the definition of the linear strain tensor

$$\varepsilon_{ij}(\mathbf{u}) = \frac{1}{2} \left( \frac{\partial v_i}{\partial x_j} + \frac{\partial v_j}{\partial x_i} \right)$$

yields:

$$\begin{aligned} \int_{\Omega_s} \rho_s \ddot{u}_i \cdot \delta u_i d\Omega_s + \int_{\Omega_s} \sigma_{ij}(\mathbf{u}) \cdot \varepsilon_{ij}(\delta\mathbf{u}) d\Omega_s \\ = \int_{\Gamma} \delta u_i \cdot \left[ -p\delta_{ij} + \mu \left( \frac{\partial v_i}{\partial x_j} + \frac{\partial v_j}{\partial x_i} \right) \right] \cdot n_j d\Gamma \end{aligned} \quad (10)$$

Finite element discretization of the integral expression yields the mass and stiffness matrices of the structure  $\mathbf{M}$  and  $\mathbf{K}$ :

$$\begin{aligned} \int_{\Omega_s} \rho_s \ddot{u}_i \cdot \delta u_i d\Omega_s \rightarrow \delta \mathbf{U}^T \mathbf{M} \ddot{\mathbf{U}} \\ \int_{\Omega_s} \sigma_{ij}(\mathbf{u}) \cdot \varepsilon_{ij}(\delta\mathbf{u}) d\Omega_s \rightarrow \delta \mathbf{U}^T \mathbf{K} \mathbf{U} \end{aligned} \quad (11)$$

where  $\mathbf{U}$  is the nodal displacement.

Discretization of the right-hand side term of equation (10) requires the calculation of the fluid stress tensor field at the fluid-structure interface. As is noted later in this article, this is achieved with the space-coupling procedure, using an interpolation of the values of pressure and velocity at the nodes of the fluid mesh which belong to the fluid-structure interface. Discretization yields the fluid forces at the fluid-structure interface:

$$\int_{\Gamma} \delta u_i \cdot \left[ -p\delta_{ij} + \mu \left( \frac{\partial v_i}{\partial x_j} + \frac{\partial v_j}{\partial x_i} \right) \right] \cdot n_j d\Gamma \rightarrow \delta \mathbf{U}^T \boldsymbol{\Phi} \quad (12)$$

The discrete structure problem is then:

$$\mathbf{M} \ddot{\mathbf{U}}(t) + \mathbf{K} \mathbf{U}(t) = \boldsymbol{\Phi}(t) \quad (13)$$

where  $\boldsymbol{\Phi}(t)$  is the generalized external forces applied at the structure surface.

In the present study, steady-state computations are performed, that is, only a static calculation of the structure is required. The inertial term then vanishes, and the structure displacements are then obtained by inverting the stiffness matrix:

$$\mathbf{U} = \mathbf{K}^{-1} \boldsymbol{\Phi} \quad (14)$$

As is detailed in the next subsection, in the experimental setup, the fixation system of the foil is rigid. For this reason, it is not considered in the calculation and a clamped condition is set on the root section, see Fig. 2. The hydrofoil is discretized with three-dimensional 10-nodes tetrahedral elements of quadratic behavior. Figure 3 shows that the asymptotic static deformation of the hydrofoil obtained by the structure calculation is reached when the number of mesh elements is greater than about 20,000. The finite element mesh used for the structure calculations contains 27,000 elements, see Fig. 4a.

The fluid problem is solved with the finite volume technique (Ferziger & Peric 1999), using the CFD code CFX. Equations (4) and (5) are integrated over the control volume  $\Omega_F$  of boundary  $\delta\Omega_F$ , using the Leibnitz rule and the Gauss theorem. The general form of

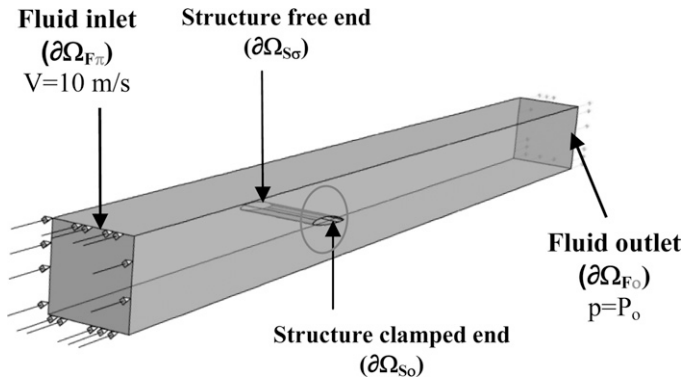


**Fig. 2** Numerical setup: fluid (test section) and structure (foil) domains and boundary conditions

an integrated conservation equation for a fluid unknown  $\phi$  (standing for any velocity field component for instance) is given by:

$$\frac{\partial}{\partial t} \left( \int_{\Omega_F} \rho_F \phi d\Omega_F \right) + \int_{\partial\Omega_F} \rho_F v_j \phi dn_j = \int_{\Omega_F} S_\phi d\Omega_F + \int_{\partial\Omega_F} \Gamma \frac{\partial \phi}{\partial x_j} dn_j \quad (15)$$

where  $S_\phi$  is the source term and  $\Gamma$  is a diffusion coefficient.

Equation (15) is discretized using a finite volume method. The fluid domain is divided into elementary fluid cells, for which an integrated conservation equation is written. Figure 4 gives a typical representation of a computational grid for a two-dimensional (2D) Cartesian problem. The time-dependent terms in equation (15) are approximated by an Euler scheme, given by:

$$\frac{\partial}{\partial t} \left( \int_{\Omega_F} \rho_F \phi d\Omega_F \right) \approx \frac{\rho_F |\Omega_F|}{\delta t} (\phi_P^{n+1} - \phi_P^n) \quad (16)$$

where  $n$  and  $n+1$  are the time steps.

The convective and diffusive terms ( $C$  and  $D$ ) are calculated using finite difference approximations, leading to the global expression:

$$\int_{\partial\Omega_P(t)} \rho_F v_j \phi - \Gamma \frac{\partial \phi}{\partial x_j} dn_j \approx \sum_M C_M^{n+1} \phi_M^{n+1} - D_M^{n+1} \phi_M^{n+1} \quad (17)$$

where  $M$  stands for the neighboring points of cell  $\Omega_P$  (see Fig. 5). Nodal values are computed with a high-resolution upwind scheme. This advection scheme is implemented into the CFD code and can be cast in the form:

$$\phi_P = \phi_{UP} + \beta \nabla \phi \Delta \vec{r} \quad (18)$$

where  $\phi_P$  and  $\phi_{UP}$  are values of  $\phi$  at the integration point  $P$  and at the upwind node (i.e., point  $W$  or  $E$  depending on the flow direction),  $\beta$  is a relaxation coefficient ranging between 0 and 1 and  $\Delta \vec{r}$  is the vector from the upwind node to the integration point  $P$ .

Taking into account equations (17) and (18) lead to the following algebraic nonlinear system formed with operators  $A$  and  $b$ :

$$A_P \phi_P^{n+1} = \sum_M A_P \phi_P^{n+1} + b_P \phi_P^n \quad (19)$$

For a detailed presentation of the finite volume method and mathematical representation of  $S_\phi$ ,  $C$ ,  $D$ ,  $A$ , and  $b$ , the reader can refer to Ferziger & Peric (1999).

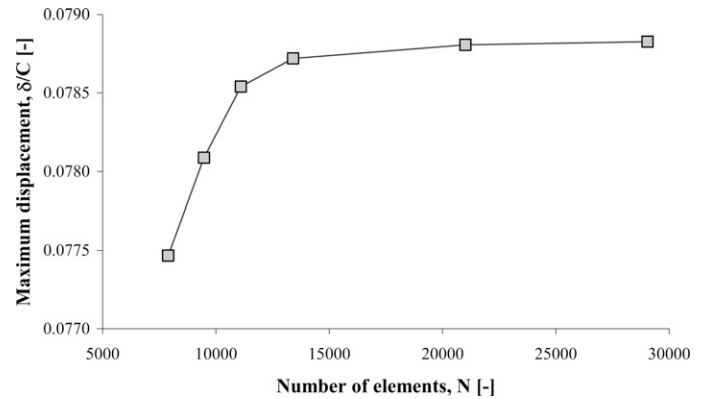


**Fig. 3** Convergence of the maximum displacement as a function of the number of mesh elements ( $V = 10$  m/s,  $\alpha = 6$  deg)

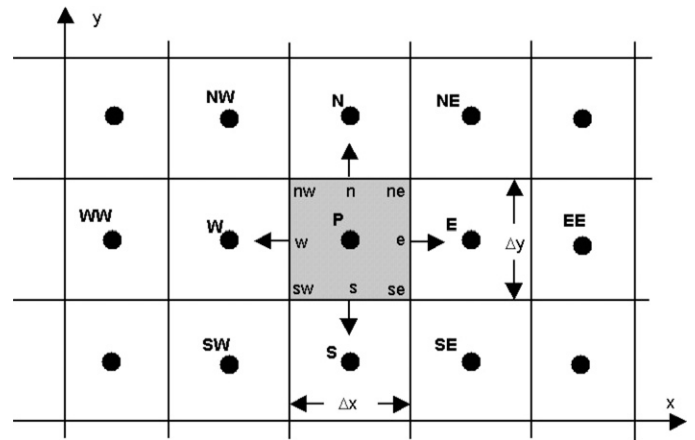


**Fig. 4** 2D Cartesian fluid computational grid

In transient analysis, equation (19) is solved with a splitting operator technique, which handles the coupling between pressure and velocity (Issa 1985); for steady computation, a similar algorithm can be used (Ferziger & Peric 1999).

The computational flow domain is presented in Fig. 2. Numerical computations are performed for a given inlet velocity of 10 m/s. A constant exit pressure condition  $P_0 = 0$  Pa is set on the outlet boundary. Symmetry conditions are set on the vertical and horizontal walls, and a wall condition is imposed on the hydrofoil. Boundary conditions at the fluid structure interface are imposed by the structure. In a general manner, the coupling condition is given by equation (9); in the present analysis, only steady-state computations are investigated, the coupling condition is  $v_i = 0$  on  $\Gamma$ .

As shown in Fig. 4c, the fluid domain is discretized with 750,000 cells. The boundary layer zone is made of 100,000 linear six-node prisms as shown in Fig. 4b, and the rest of the domain is discretized with 650,000 linear four-node tetrahedrons. Although the mesh is relatively coarse on both pressure and suction sides, it was found to be reliable according to lift coefficient convergence shown in Fig. 6. The number of elements has been modified linearly in the near wall region in the three directions. A high discretization level at the leading edge



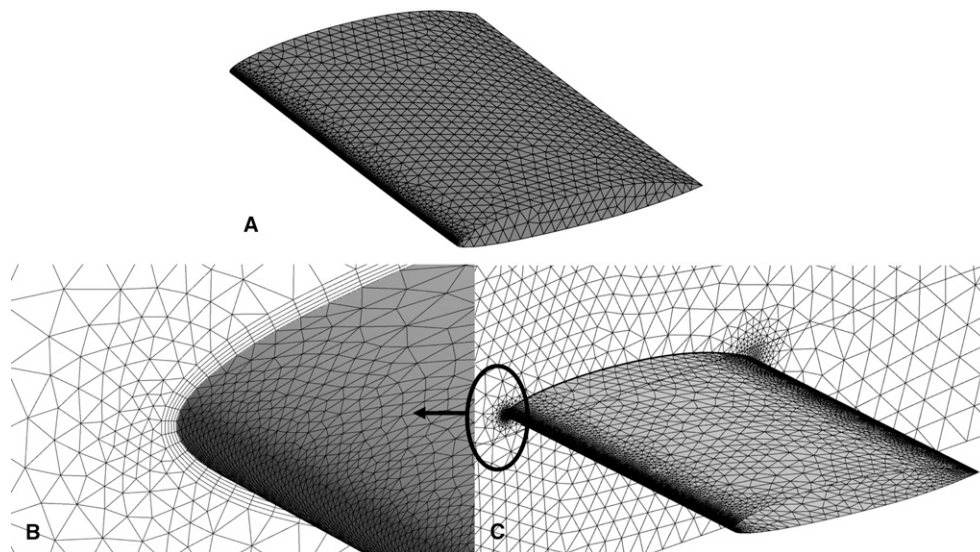


**Fig. 5** a Structure mesh, b, and c fluid mesh: hydrofoil and lateral wall surface meshes

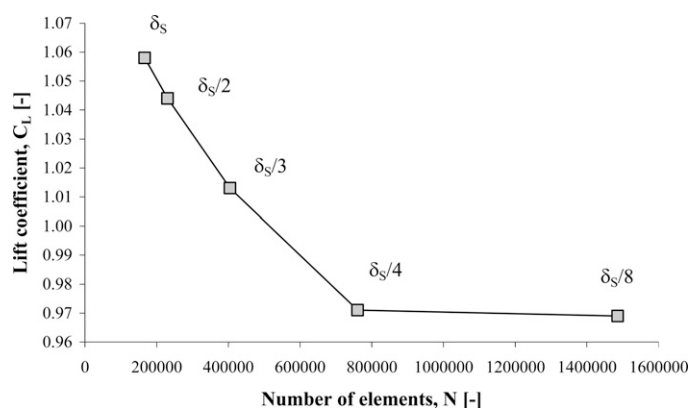


**Fig. 6** Convergence of the lift coefficient as a function of the number of mesh elements ( $V = 10$  m/s,  $\alpha = 6$  deg).  $\delta_s$  is the node spacing at the hydrofoil surface

is necessary to capture large pressure gradients. Therefore, the foil is decomposed into five zones to control the mesh density. The mesh of the foil section is made of 30 elements in the leading edge zone, 20 elements in the trailing edge zone, and 20 elements for the pressure side region and the suction side region, respectively. The turbulence model  $k-\omega$  SST (Menter 1994) is applied for the flow resolution, and the boundary layer is modeled with a wall function ( $y^+$  between 20 and 100). The tip clearance between the hydrofoil and the vertical tunnel wall is not taken into account. A free sliding condition is imposed at the tip section that allows displacements only in the plane of the adjacent vertical wall.

For each flow condition, two types of simulation are performed, namely “noncoupled” (Fig. 7a) and “coupled” (Fig. 7b) calculations.

- In noncoupled computations, the hydrodynamic loading is first computed on the hydrofoil considered as rigid and is transferred into the CSD code. A CSD computation is then performed and yields the static solution.

- In coupled computations, an iterative procedure (see the example of cardiovascular device simulation by Penrose & Staples 2001) is used in order to reach convergence on the coupled problem by balancing the energy exchanges at the fluid-structure interface.

During the coupled computation, the CFD and the CSD problems are solved alternatively through an iterative algorithm described in Fig. 7b (Sigrist & Abouri 2006). The fluid-structure coupled procedure is initialized with a steady CFD solution obtained on the hydrofoil considered to be rigid. The hydrodynamic loading resulting from the pressure field obtained at the fluid-structure interface is transferred into the CSD code using the conservative interpolation procedure implemented into the ANSYS solver. This ensures that a total quantity passing across the interface is conserved. Then, the structural response of the hydrofoil is computed. Nodal structure displacements are mapped on the CFD mesh control points at the interface with the profile preserving interpolation procedure implemented into the ANSYS solver. This ensures at the interface that all nodes on the CFD side query the CSD surface. Then the entire CFD domain is meshed again, and the process is repeated until convergence is reached. A thorough discussion on the various numerical techniques for CFD/CSD code coupling is beyond the scope of the present paper; detailed insights on coupling techniques in space/in time can be found in Maman and Farhat (1995), Farhat et al. (1998b), Tezduyar et al. (2006), and van Zuijlen et al. (2007). In the present case, the moving mesh technique is based on an elastic structure behavior analogy in order to control mesh distortions close to the deformable surface. A dynamic stiffness is applied on the CFD grid, and a spring analogy remeshing method is used (Farhat et al. 1998a, Aquelet et al. 2005, Markous et al. 2007). A new CFD computation can be started again at the current iteration; the process is repeated until convergence is reached. A residual-based criterion is used in the CFD solver. Moreover, a physical criterion based on the convergence of the maximum vertical displacement is added to ensure the convergence of the coupled solution. The evolution of the maximum displacement

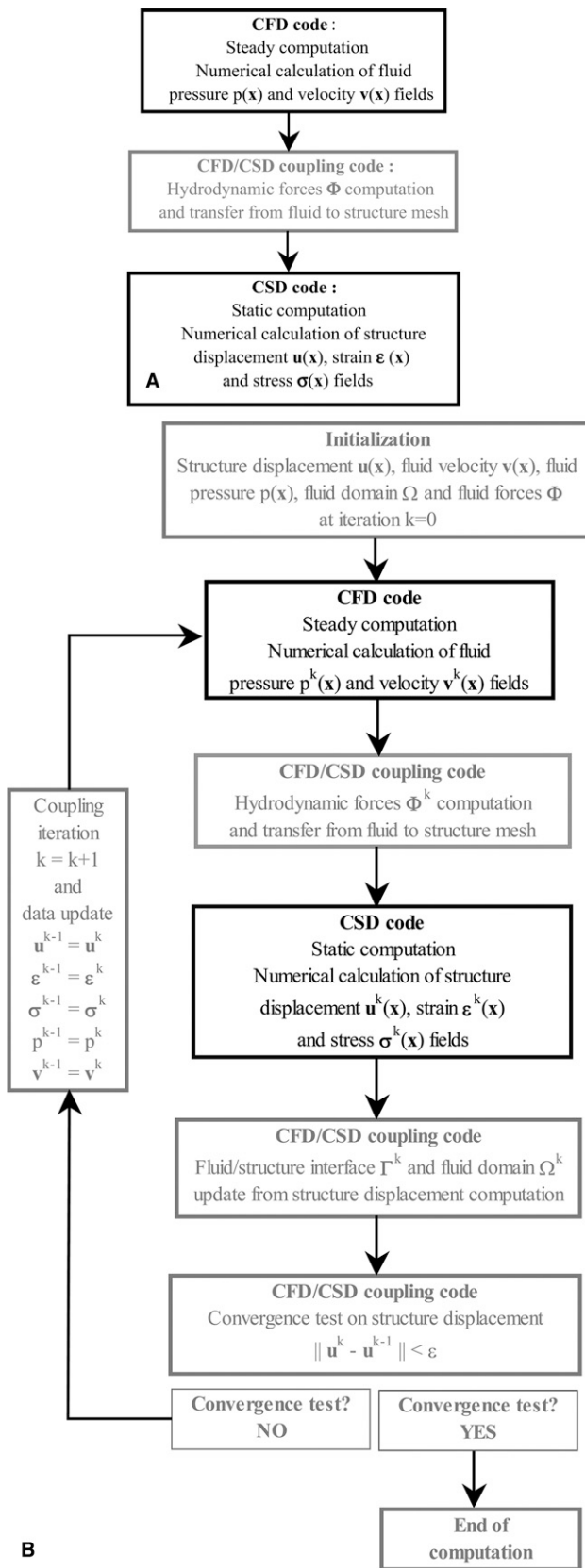


Fig. 7 a Noncoupled CFD/CSD calculation; b Coupled CFD/CSD calculation

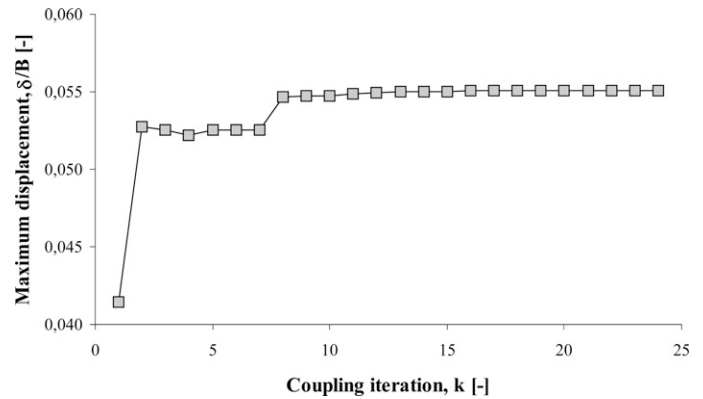


Fig. 8 Maximum displacement convergence versus iterations number

during the coupled CFD-CSD computation is presented in Fig. 8; about 10 iterations or so are needed to reach convergence.

Computations are performed with a PC Xeon dual core 2.4 GHz with 4Go Ram. Table 1 shows the CPU total time needed to reach convergence for coupled computation which is nine times longer than noncoupled computation. Of the total CPU time, 84% is used for the CFD resolution; 22% of the CFD CPU time is used for the remeshing of the CFD domain.

### 3. Experimental setup

Measurements are carried out in the cavitation tunnel at IRE-Nav. The experimental setup is described in Figs. 9 and 10. The hydrofoil is mounted horizontally at midheight in the 192 mm squared test section of the hydrodynamic tunnel. The hydrofoil is a rectangular cambered wing with a section based on the NACA66 family that presents a camber-type NACA  $a = 0.8$ , a camber ratio of 2%, and a relative thickness of 12% (Leroux et al. 2005). The chord length is  $C = 150$  mm, and the span is  $B = 191$  mm. Theoretical zero lift angle  $\alpha_0$  is equal to  $-2.35$  deg.

A plastic material (POM polyacetate, see characteristics on Table 2) is selected in order to obtain a static deflection magnitude equal to 10% of the chord length at the tip section. In the early stage of the project, basic computations have permitted estimation of the maximal operating conditions according to the material elastic limit. The incidence is  $\alpha = 6$  deg and the upstream velocity  $V = 10$  m/s; under these conditions, the maximum stress in the POM hydrofoil is 40 MPa.

As shown in Fig. 2, the hydrofoil is fixed on one of the test section lateral walls. The hydrofoil root section is clamped, and the tip section is free. A protractor is then used to set the angle of incidence. The horizontal plane is used to set the zero incidence. The rotation axis is located at  $x/C = 0.5$ , and the seal is ensured by a thoracic joint.

Experiments are performed with a visual system to estimate the tip section displacement. Measurements are carried out by taking two lateral pictures of the nondeformed and deformed tip section. The two pictures are compared by the help of an image processor to estimate the hydrofoil displacement.

Experiments are carried out in an extended range of upstream velocities (from 0 to 10 m/s, which corresponds to Reynolds number ranging from  $0.75 \times 10^6$  to  $1.5 \times 10^6$ ) and angle of incidence of 0, 2, 4, and 6 deg.

**Table 1 CPU total time for noncoupled and coupled computations**

	Noncoupled computation			Coupled computation			
	CFD initial	CSD static	Total	CFD initial	CFD coupled	CSD coupled	Total
CPU time (s)	1026	30	1056	1026	8044	540	9610



**Fig. 9** Experimental setup. Hydrodynamic tunnel test section

A numerical camera is used to get a side view of the hydrofoil and then measure the free tip section displacement. The camera is placed on a tripod at hydrofoil level, and lighting is set to obtain the most luminous and clearest section. The focal distance is regulated on this section. In order to be sure that the camera does not move during the measurements, two reference crosses are drawn on the Plexiglas wall.

A first picture with  $V = 0$  m/s is taken as the reference. Then, for each velocity condition, three images are taken to observe possible vibrations of the structure. Once maximum velocity is reached, the procedure is carried out in the opposite way until the upstream velocity is decreased to 0 m/s. The comparison between initial and final pictures is used to check that the hydrofoil is back to its initial position, ensuring that the deformation is elastic.

The acquisition was improved by marking the hydrofoil with 11 reference points distributed along the chord to have the section displacement. It is numbered from point # 1 located at the leading edge ( $x/C = 0.0$ ) to point # 11 located at the trailing edge ( $x/C = 1.0$ ). The displacements of the leading edge and the trailing edge points in each section allow determination of the relative vertical structure deflection along the span.

The image postprocessing enables the measurement of the foil displacement at the free tip section by comparing deformed hydrofoil to initial hydrofoil ( $V = 0$  m/s taken as a reference pattern). Structure displacements  $\delta_x$  and  $\delta_y$  on  $X$  and  $Y$  axis between pictures No. 1 and 2 are then given by  $\delta_x = x_2 - x_1$  and  $\delta_y = y_2 - y_1$ .

The incidence variation of the free tip section is then defined as:

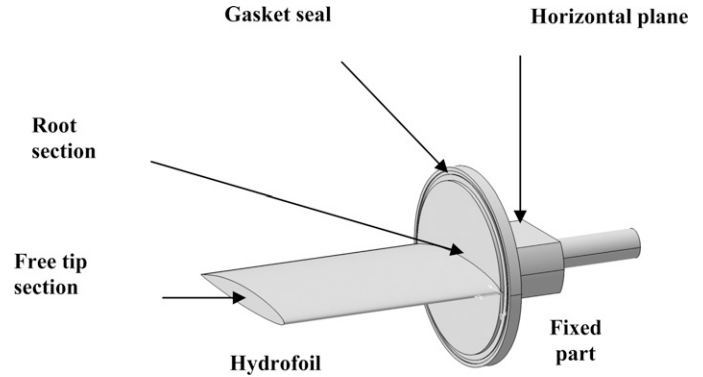


**Fig. 10** Experimental setup. Hydrofoil design

**Table 2 Hydrofoil POM material properties**

Young modulus $E$ (MPa)	Density $\rho_s$ (kg/m <sup>3</sup> )	Poisson coefficient $\nu$	Elastic resistance $\sigma_E$ (MPa)
3000	1480	0.35	70

$$\Delta\alpha = \arctan\left(\frac{\delta_{y\text{-leading}} - \delta_{y\text{-trailing}}}{C}\right) \quad (20)$$

with  $\delta_{y\text{-leading}}$  the leading edge vertical displacement and  $\delta_{y\text{-trailing}}$  the trailing edge vertical displacement.

During the experiments, it was observed that the camera was not fully located in the horizontal plane of the tunnel test section, which led to a correction on the level of the angle of incidence of  $\Delta\alpha + 0.5$  deg compared with the original pictures. In order to make sure that this variation was due to the camera, the tunnel was drained at half test section, and it was checked that the hydrofoil chord was well aligned with the horizontal free surface.

The image-processing uncertainties are taken into account in the measurement procedure. It corresponds to the precision of the method used to capture the pixel location of each marking point. Reading uncertainty is about 2 pixels, that is to say  $\pm 1$  pixel. Since the chord is 651 pixels long for a real size of 150 mm, 1 pixel equals 0.23 mm, and the uncertainty on measured displacements is  $\Delta_{\text{pixel}} = 0.46$  mm. Corresponding dimensionless uncertainties are  $\Delta_x/C = 0.0031$  in  $X$  axis direction and  $\Delta_y/B = 0.0024$  in  $Y$  axis direction. Uncertainties for the angle of incidence and twist measurement are then evaluated with equation (20), yielding:

$$\Delta(\Delta\alpha) = \arctan\left(\frac{\Delta_{\text{pixel}}}{C}\right) \times \frac{360}{2\pi} = 0.178 \text{ deg}$$

#### 4. Influence of fluid-structure coupling

The structure deformations and the hydrodynamic loadings are investigated through a comparison of coupled and noncoupled calculations.

##### 4.1. Hydrofoil deformation analysis

The deformations of the foil are expected to be three dimensional, which makes the geometrical analysis rather difficult.



However, the decomposition of the total displacement into elementary displacement modes is useful in the context of lifting bodies. According to Patil and Hodges (2004), the pressure distribution is essentially affected by twist modification. Therefore, a decomposition of the total displacement into three components is performed:

- Vertical displacement along the  $Y$  axis, which is the main component of the total displacement
- Twist, defined as the evolution of the local incidence along the span  $Z$  axis. In each section, the local incidence definition is based on the difference between the leading edge and the trailing edge positions
- Skew, corresponding to the structure horizontal displacement along the  $X$  axis. However, it was observed that the magnitude of the skew is much lower than the magnitudes of vertical displacement and twist. For this reason, the skew will not be analyzed.

The vertical displacements obtained on the suction side by the coupled computations are presented in Fig. 11a. It is observed that the maximum displacement is located at the foil tip in the vicinity of the leading edge and is about 8.5% of the chord length for the considered flow conditions. Figure 12 presents the vertical displacements calculated at the leading edge and at the trailing edge in the six equally spaced sections presented in Fig. 11b. The leading edge vertical displacement  $\delta_{y\text{-leading}}$  is higher than the trailing edge displacement  $\delta_{y\text{-trailing}}$ , resulting in a twist deformation of the hydrofoil.

Taking a twist reference value of zero at the nondeformed root section, the local variation of the incidence along the span can be evaluated using equation (20).

The results are presented in Table 3. As mentioned previously, the local incidence increases continuously from 0 deg at the root section ( $z/B = 0$ ) to the maximum value of 0.83 deg at the tip section ( $z/B = 1$ ).

#### 4.2. Hydrofoil pressure distribution analysis

As far as the hydrodynamic effects of the coupling are concerned, the study focuses on local and global hydrodynamic loadings, respectively, given by the pressure coefficient:

$$C_P(x) = 2 \times \frac{P(x) - P_o}{\rho_F V^2} \quad (21)$$

and the lift coefficient:

$$C_L = 2 \times \frac{L}{\rho_F V^2 S} \quad (22)$$

where  $L$  is the vertical force applied on the hydrofoil,  $P_o$  is the pressure reference,  $V$  is the free stream velocity, and  $S = C \times B$  is the hydrofoil reference surface.

The effect of the structure deformation on the local hydrodynamic loadings has been investigated with coupled and noncoupled computations. The results are compared in Fig. 13, which shows the pressure distributions obtained at the root and at the tip sections. In the leading edge vicinity of the tip section, the absolute value of the minimal pressure coefficient predicted by the coupled computation is higher than the one obtained by the noncoupled computation. Both coupled and noncoupled pressure coefficient predictions tend to be equal at about  $x = C/2$ .

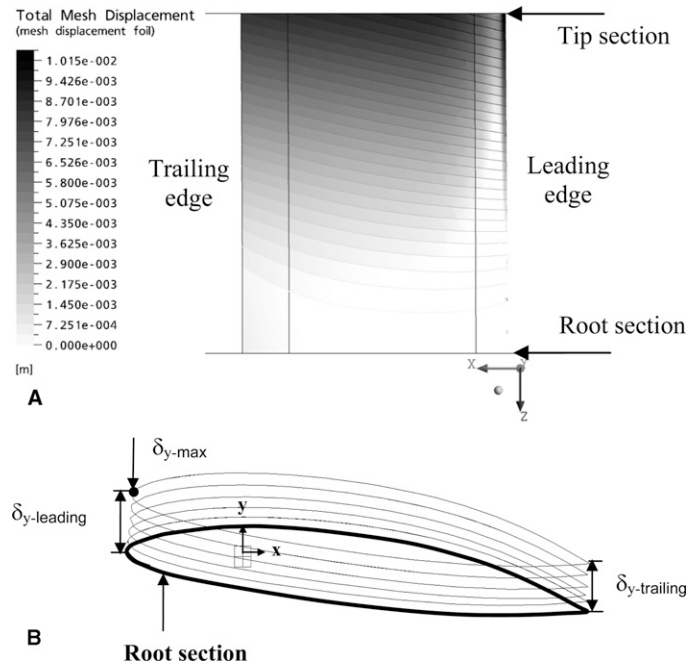


Fig. 11 Coupled computation with  $V = 10$  m/s,  $\alpha = 6$  deg. a Vertical displacement magnitude (m) on the suction face. b Side view of six equally spaced sections (step  $z/b = 0.2$ )

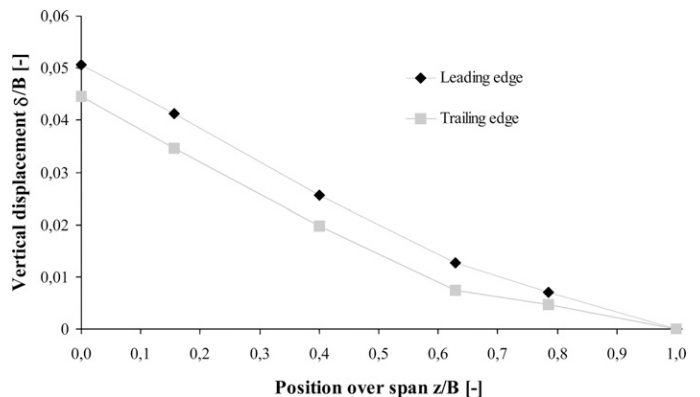


Fig. 12 Leading edge and trailing edge vertical displacements (coupled computation)

This difference results from the increase of the angle of incidence due to the twist which is caused by pressure and thickness distributions along the chord. In spite of the important foil thickness close to the leading edge region, the concentration of the higher pitching elementary moments in this region induces the leading edge zone to deflect more than the trailing edge zone. The pressure distribution is approximately the same on the nondeformed root section as the one obtained in the rigid case (noncoupled computation); the slight difference can be attributed to three-dimensional (3D) effects induced by the structure deformations.

The quality of the mesh at the leading edge allows determination of the minimal pressure values accurately. As shown in Fig. 13, there is a net difference between the two cases: coupled



**Table 3** Local incidence variation along the span (twist law).  
Coupled computation

Span ( $z/B$ )	0.00	0.20	0.40	0.60	0.80	1.00
$\Delta\alpha$ (deg)	0.00	0.20	0.51	0.66	0.80	0.83

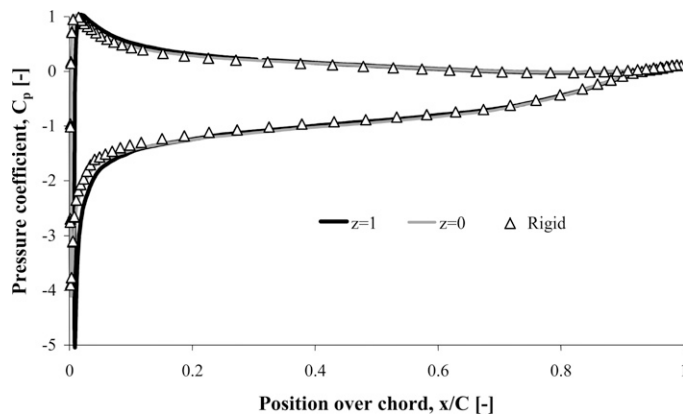


**Fig. 13** Pressure coefficient distributions along the hydrofoil chord for two span locations ( $V = 10$  m/s,  $\alpha = 6$  deg)

computation leads to  $C_{p_{\min}} = -4.8$ , whereas rigid computation leads to  $C_{p_{\min}} = -3.8$ . No cavitation has been observed during experiments at the operating conditions, but this difference could have a significant impact on cavitation inception concerning hydrodynamic applications (Hauville et al. 1999, Deniset et al. 2002). In Fig. 14, additional sections located between the root and the tip show the evolution of the pressure along the span. The absolute minimal pressure increases proportionally to the local incidence variation induced by the deformations.

Numerical computations are extended to other angles of incidence ranging from 0 to 6 deg for free stream velocities equal to 5 and 10 m/s. Maximum displacement and lift coefficient are investigated for coupled and noncoupled computations. The coupling effect can be clearly observed in Fig. 15, which sketches the maximum displacement as a function of the angle of incidence: it can be observed that the displacement evolves linearly as a function of the angle of incidence for both computations.

For  $V = 10$  m/s in “coupled” computations, the vertical displacement is larger than in the “noncoupled” computations; the difference increases with the angle of incidence. At an angle of incidence  $\alpha = 6$  deg,  $\delta_{y,\max} = 0.056$  in the coupled case against  $\delta_{y,\max} = 0.051$  in the noncoupled case (which represents a variation of about 10%). This result is in agreement with the pressure coefficient modification, as a result of the hydrofoil twist. Besides, the hydrodynamic forces applied on the hydrofoil are larger in the “coupled” computation, thus increasing the deformation. The lift coefficient is also found to vary linearly as a function of the maximum vertical displacement. Numerical simulations for  $V = 5$  m/s show that the effect of the coupling increases together with upstream velocity. At  $\alpha = 6$  deg, coupled computation lead to an increase of both deflection and lift coefficient, of about 3.5% and 1.5%, respectively. In that case, there is a significant twist ( $\alpha = 6$  deg; see Table 4), but the loading is less important ( $V = 5$  m/s), which tends to reduce coupling effects.

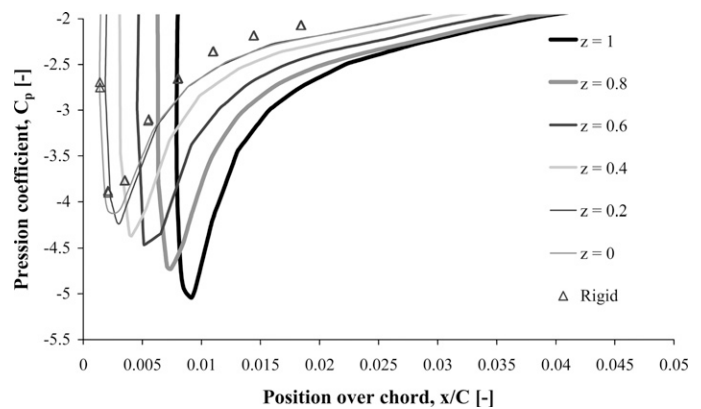


**Fig. 14** Pressure coefficient distributions along the hydrofoil chord for different span locations ( $V = 10$  m/s,  $\alpha = 6$  deg). Detailed data in the range  $-5.5 < C_p < -2.0$

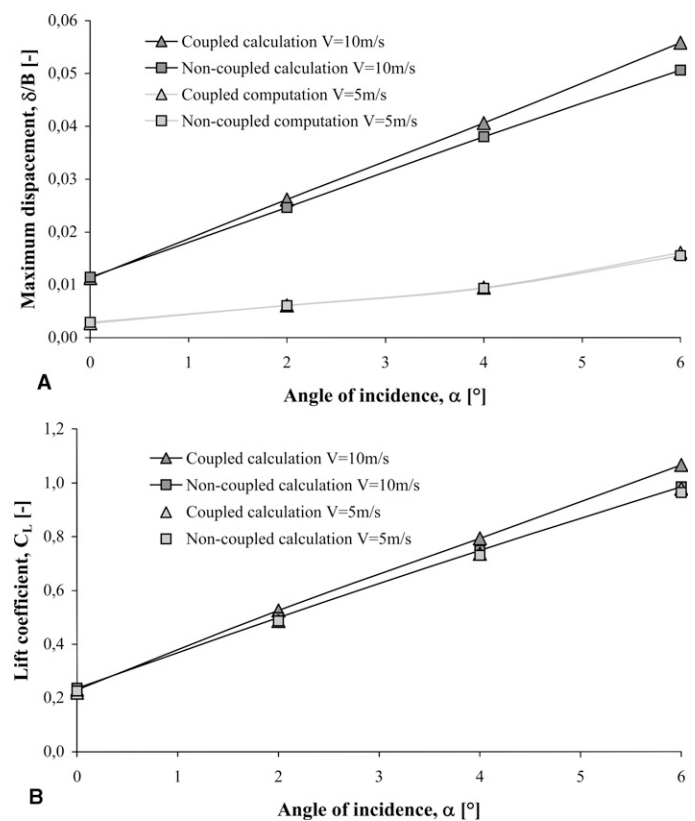


**Fig. 15** Maximum vertical displacement and lift coefficient for various angles of incidence ( $V = 5$  and 10 m/s)

## 5. Discussion on numerical and experimental results

As pointed out previously, the structure deformation has a significant impact on the hydrodynamic coefficients, which is a key issue in the understanding of the influence of fluid-structure interaction in the hydrodynamics of the foil. In this section, experimental displacements measurements are exposed and compared with numerical computations. Figure 16a shows a superpo-

**Table 4** Hydrofoil vertical displacement along the chord ( $\alpha = 6$  deg,  $V = 10$  m/s)

Point No.	1	2	3	4	5	6	7	8	9	10	11
$\Delta y$ (mm)	10.82	10.34	9.64	9.87	9.87	9.4	9.17	8.93	8.93	7.99	8.46

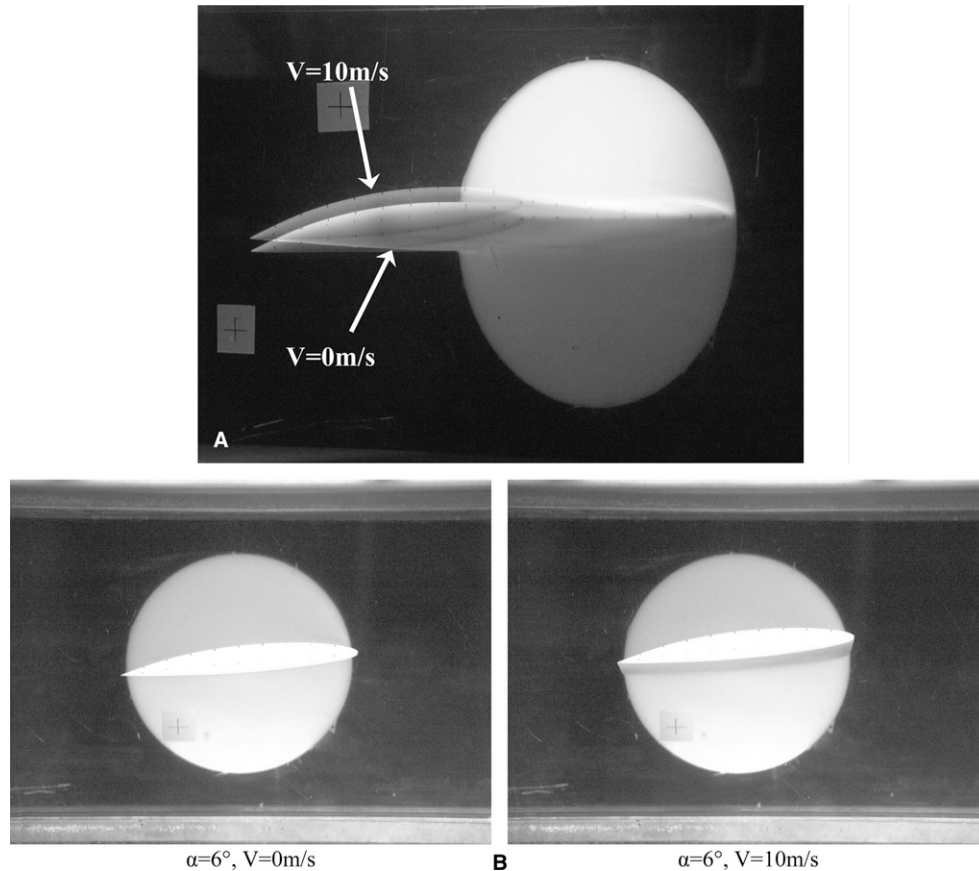


**Fig. 16** Displacement of the hydrofoil at  $\alpha = 6$  deg. *a* Perspective view. *b* Side views

sition of two pictures of the foil, respectively at 0 m/s (nondeformed) and 10 m/s (deformed) as an illustration of the experimental results.

Figure 16*b* shows two photographs of the nondeformed (left) and deformed (right) hydrofoil (the flow comes from the right); as shown, displacements are noticeable through the shadow region.

### 5.1. Tip section displacement

Figure 17 shows experimental results for  $\alpha = 6$  deg and various upstream velocities. It can be concluded that the structure moves vertically, as a consequence of the lift effect. Twist is observed by measuring the difference between leading edge and trailing edge displacements. Table 4 shows the difference between vertical displacements obtained for upstream velocities of 0 and 10 m/s. Maximum displacement is obtained at the leading edge (point # 1) while minimum displacement is obtained at the trailing edge (point # 11). The twist is given by  $\Delta y_1 - \Delta y_{11} = 2.36 \pm 0.115$  mm; the resulting local incidence variation is then given:

$$\Delta i = \arctan\left(\frac{2.36}{C}\right) \times \frac{360}{2\pi} = 0.81 \text{ deg}$$

Figure 18 gives the evolution of the maximum vertical displacement as a function of the upstream velocity. It is noticed that displacement increases as the square of the velocity for the different angles of incidence considered. Numerical displacement as a function of velocity can be deduced from numerical lift coefficient  $C_L$  by the following relation  $y/B(\alpha, V) = KC_L(\alpha) \times V^2$ , where  $K$  is a constant (the estimated displacements are represented by parabolic dotted curves in Fig. 18).

### 5.2. Comparison of numerical and experimental results

The experimental tests carried out with an upstream velocity of 10 m/s are compared with numerical noncoupled and coupled calculations. The clamped root section is taken as the reference for both measurements and computations. The hydrofoil deformation is accurately predicted by both the noncoupled and coupled computations as shown in Fig. 19, where a good agreement be-

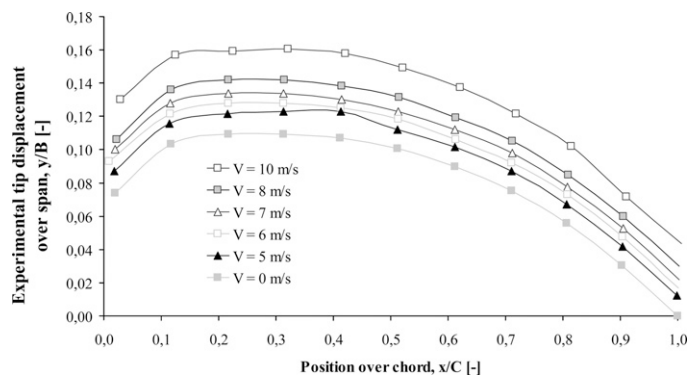


Fig. 17 Tip section displacement for various upstream velocities ( $\alpha = 6$  deg, suction side)

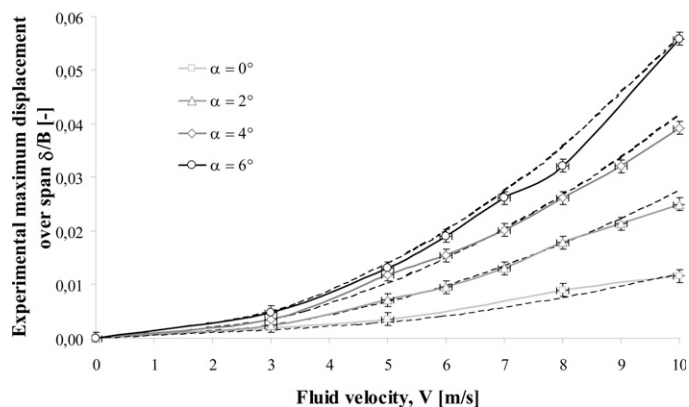


Fig. 18 Maximum vertical displacement versus upstream velocity for different angles of incidence

tween numerical results and measurements is observed. In this figure, error bars cannot be shown because they are much lower (see uncertainty calculation in section 3) than the symbols used. Based on this consideration, tip section displacement is better predicted by coupled computation. Experimental and numerical local incidences are deduced from tip section displacement in Table 5.

For an upstream velocity of 10 m/s, the difference between experimental and numerical local incidence variation is of about 2.1%.

Experimental maximum displacement  $\delta_y/B$  as a function of incidence is compared with numerical predictions (for the various angles of incidence 0, 2, 4, and 6 deg) in Fig. 20. The results obtained from viscous computations are close to the measurements. The coupling effect is weak for small angles of incidence and relatively low upstream velocities ( $V = 5$  m/s). Consequently, maximum displacement is also well predicted by noncoupled viscous computations. Table 5 shows that the twist is weak and well predicted for both coupled and noncoupled computations. Coupled computations show a higher twist deformation in all cases compared with noncoupled computation. However, the coupling effect cannot be clearly identified through measurements since the uncertainty is of the same order than the difference between coupled and noncoupled computation. Conversely, for larger angles of incidence and larger upstream velocities ( $V = 10$  m/s),

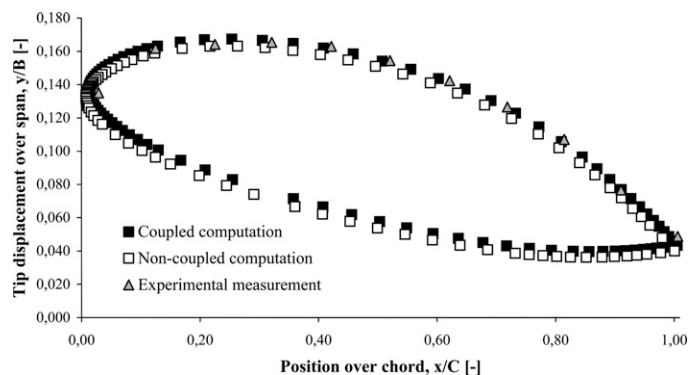


Fig. 19 Experimental and numerical tip section displacements ( $\alpha = 6$  deg,  $V = 10$  m/s)

Table 5 Variation of the local incidence in the free tip section as a function of the angle of incidence ( $V = 10$  m/s) and as a function of the upstream velocity ( $\alpha = 6$  deg). ( $\alpha\Delta$ ) = 0.18 deg

$\alpha$ (deg)		0	2	4	6	
$\Delta\alpha$ (deg)	Experimental	–	0.09	0.41	0.81	
	Coupled computation	–0.06	0.24	0.54	0.83	
	Noncoupled computation	–0.04	0.22	0.49	0.76	
$V$ (m/s)		5	6	7	8	10
$\Delta\alpha$ (deg)	Experimental	0.26	0.33	0.57	0.66	0.81
	Coupled computation	0.19	0.28	0.39	0.52	0.83
	Noncoupled computation	0.19	0.27	0.37	0.48	0.76

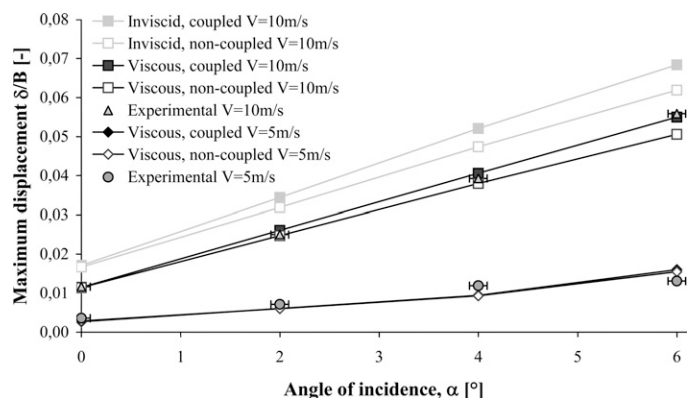


Fig. 20 Maximum displacement versus incidence ( $V = 5$  m/s and  $V = 10$  m/s). Comparison of inviscid and viscous coupled/noncoupled calculations with experimental results

displacements are well predicted by coupled computations, highlighting the importance of taking into account the fluid-structure coupling effect. In addition, Euler computations for 10 m/s have been performed to quantify the influence of fluid viscosity. As expected, inviscid fluid computations lead to higher values of  $\delta_y$  than viscous fluid computations. Finally, it can be noticed that for Euler and viscous computations, the underestimations of the displacement by noncoupled computations compared with coupled ones are quite the same.

## 6. Conclusion

The hydroelastic behavior of a deformable hydrofoil has been investigated through a comparison of numerical and experimental results. In particular, the following conclusions have been pointed out:

- The hydrofoil deformations are accurately predicted by the coupled computations. The maximum displacement is located at the leading edge at the foil tip section. The local incidence increases continuously from 0 at the root section to the maximum value at the tip section. It has been furthermore noticed that displacement increases as the square of the velocity for the different angles of incidence considered.
- The hydrodynamic forces have been found to be strongly linked to the structure deformations. The lift coefficient varies linearly as a function of the maximum structure vertical displacement. The absolute minimum pressure coefficient at the leading edge increases proportionally to the local incidence variation induced by the deformations. This should have a strong impact on cavitation inception in the tip section; such a result is of paramount importance for naval applications.
- The importance of the fluid-structure coupling process for accurate force predictions has been underlined. The hydrodynamic loading is strongly related to foil deformation. Indeed, when compared with noncoupled computation for  $V = 10$  m/s and  $\alpha = 6$  deg, coupled computation leads to a 10.7% increase of the maximum vertical displacement and a 10.6% increase of the lift coefficient. Structure displacements and lift evolutions are in the same ratio, as a major consequence of the twist amplification. For small angles of incidence and low upstream velocities, the coupling influence is weak. Then a noncoupled computation is relevant since it is nine times faster than a coupled computation.

The presented work has shown that a coupled fluid structure study can be really useful for naval applications; CSD and CFD code coupling procedures have been proved robust enough to consider more complex FSI studies. Applications of this numerical approach are currently under investigation for the analysis of propellers or ship stabilizers vibrations in transient turbulent regimes or cavitating conditions.

## Acknowledgment

The authors gratefully acknowledge the technical staff of IRE-Nav for its contribution to the experimental setup.

## References

- AQUELET, N., SEDDON, C., SOULI, M., AND MOATAMED, M. 2005 Initialisation of volume fraction in fluid-structure interaction problem, *International Journal of Crashworthiness*, **10**, 3, 237–247.
- AXISA, F. 2006 *Modelling of Mechanical Systems, Vol. 3: Fluid-Structure Interaction*, Elsevier.
- BHARDWAJ, M. K. 1997 *A CFD/CSD Interaction Methodology for Aircraft Wings*, PhD thesis, Virginia Polytechnic Institute and State University, Blacksburg, VA.
- DENISET, F., NAVAZA, V., BILLARD, J. Y., AND HAUVILLE, F. 2002 Investigations of tip vortex cavitation inception (TVC) on hydrofoils deduced from propeller blades, *Proceedings, Fifth Numerical Towing Tank Symposium NuTTS'2002*, 29 September–1 October, Pornichet, France.
- ELLER, D., AND HEINZE, S. 2005 Approach to induced drag reduction with experimental evaluation, *Journal of Aircraft*, **42**, 6, 1478–1485.
- ENGEL, M., AND GRIEBEL, M. 2004 *Flow Simulation on Moving Boundary-Fitted Grids and Application to Fluid-Structure Interaction Problems*, Institute of Numerical Simulation, University of Bonn, Wegelestr.
- FARHAT, C., DEGAND, C., KOOBUS, B., AND LESOINNE, M. 1998a Torsional springs for two-dimensional dynamic unstructured fluid meshes, *Computer Methods in Applied Mechanics and Engineering*, **163**, 231–245.
- FARHAT, C., LESOINNE, M., AND MAMAN, N. 1995 Mixed explicit/implicit time integration of coupled aeroelastic problems, *International Journal for Numerical Methods in Fluids*, **21**, 807–835.
- FARHAT, C., LESOINNE, M., AND LE TALLEC, P. 1998b Load and motion transfer algorithm for fluid-structure interaction problems with non-matching discrete interfaces: momentum and energy conservation, optimal discretization and application to aeroelasticity, *Computer Methods in Applied Mechanics and Engineering*, **157**, 95–114.
- FERZIGER, J. H., AND PERIC, M. 1999 *Computational Methods for Fluid Dynamics*, Springer-Verlag.
- GIBERT, R. J. 1986 *Vibration des structures. Interaction avec les fluides. Sources d'excitation aléatoires*, Collection de la Direction des Etudes et Recherches d'Electricité de France, vol. 69, Eyrolles.
- HAUVILLE, F., DENISET, F., BILLARD, J. Y., NAVAZA, V., AND LE SOUDÉER, J. L. 1999 Influence of the propeller blade geometry on the tip vortex cavitation, *Proceedings, International Conference on Propeller Cavitation NCT'50*, 3–5 April, University of Newcastle upon Tyne, England.
- ISSA, R. I. 1985 Solution of the implicitly discretised fluid flow equation by operator splitting, *Journal of Computational Physics*, **62**, 40–65.
- KUO, J., AND VORUS, W. 1985 Propeller blade dynamic stress, *Proceedings, 10th Ship Technology and Research (STAR) Symposium*, Norfolk, VA.
- LEROUX, J.-B., COUTIER-DELGOSHA, O., AND ASTOLFI, J. A. 2005 A joint experimental and numerical study of mechanisms associated to instability of partial cavitation on two-dimensional hydrofoil, *Physics of Fluids*, **17**, 052101.1–052101.20.
- LIN, H., AND LIN, J. 1996 Nonlinear hydroelastic behavior of propellers using a finite element method and lifting surface theory, *Journal of Marine Science and Technology*, **1**, 114–124.
- LUND, E., MOLLER, H., AND JAKOBSEN, L. A. 2001 Shape design optimization of steady fluid-structure interaction problems with large displacements, *Proceedings, 42nd AIAA/ASME/ASCE/AHS/ASC Structures, Structural Dynamics, and Materials Conference and Exhibit (SDM)*, Seattle, WA, AIAA Paper 2001-1624.
- MAMAN, M., AND FARHAT, C. 1995 Matching fluid and structure meshes for aeroelastic computations: a parallel approach, *Computers & Structures*, **54**, 779–785.
- MACKERLE, J. 1999 Fluid-structure interaction problems, finite element approach and boundary elements approaches. A bibliography, *Finite Elements in Analysis and Design*, **31**, 231–240.
- MARKOUS, G. A., MOUROUTIS, Z. S., AND CHARMPI, D. C. 2007 The ortho-semi-torsional (OST) spring analogy method for 3D moving boundary problems, *Computer Methods in Applied Mechanics and Engineering*, **196**, 747–765.
- MENTER, F. R. 1994 Two-equation eddy-viscosity turbulence models for engineering applications, *AIAA Journal*, **32**, 8, 1598–1605.
- MORAND, H. J.-P., AND OHAYON, R. 1995 *Fluid Structure Interaction*, Wiley & Sons.
- PAÏDOUSSIS, M. P. 1998 *Fluid-Structure Interaction: Slender Structures and Axial Flows*, Vol. 1, Elsevier.
- PAÏDOUSSIS, M. P. 2003 *Fluid-Structure Interaction: Slender Structures and Axial Flows*, Vol. 2, Elsevier.
- PATIL, M. J., AND HODGES, D. H. 2004 On the importance of aerodynamic and structural geometrical nonlinearities in aeroelastic behavior of high-aspect-ratio wings, *Journal of Fluids and Structures*, **19**, 905–915.
- PENROSE, J. M. T., AND STAPLES, C. J. 2001 Implicit fluid-structure coupling for simulation of cardiovascular problems, *International Journal for Numerical Methods in Fluids*, **1**, 1–13.
- PIPERNO, S., FARHAT, C., AND LARROUTOUROU, B. 1995 Partitioned procedures for the transient solution of coupled aeroelastic problems. Part I: model problem, theory and two-dimensional application, *Computer Methods in Applied Mechanics and Engineering*, **1–2**, 124, 79–112.
- PIPERNO, S. 1997 Explicit-implicit fluid-structure staggered procedures with a structural predictor and fluid subcycling for 2D inviscid aeroelastic simulations, *International Journal for Numerical Methods in Fluids*, **25**, 10, 1207–1226.
- PIPERNO, S., AND FARHAT, C. 2001 Partitioned procedures for the transient solution of coupled aeroelastic problems. Part II: energy transfer analysis



- and three-dimensional application, *Computer Methods in Applied Mechanics and Engineering*, **190**, 3147–3170.
- SCHÄFER, M., AND TESCHAUER, I. 2001 Numerical simulation of coupled fluid-solid problems, *Computer Methods in Applied Mechanics and Engineering*, **190**, 3645–3667.
- SEND, W. 1999 Coupling of fluid and structure for transport, aircraft wings, *Proceedings, International Forum on Aeroelasticity and Structural Dynamics*, 22–25 June, Williamsburg, VA.
- SIGRIST, J. F., AND ABOURI, D. 2006 Numerical simulation of a non-linear coupled fluid-structure problem with implicit and explicit coupling procedure, *Proceedings, Pressure Vessel and Piping*, 23–27 July, Vancouver, Canada.
- TEZDUYAR, T. E., SATHE, S., KEEDY, R., AND STEIN, K. 2006 Space-time finite element techniques for computation of fluid-structure interactions, *Computer Methods in Applied Mechanics and Engineering*, **195**, 2002–2027.
- YOUNG, Y. L., MICHAEL, T. J., SEAVER, M., AND TRICKEY, S. T. 2006 Numerical and Experimental Investigations of Composite Marine Propellers, *Proceeding, 26th Symposium on Naval Hydrodynamics*, Rome, Italy, September 17–22.
- YOUNG, Y. L. 2007 Time-dependent hydroelastic analysis of cavitating propulsors, *Journal of Fluids and Structures*, **23**, 269–295.
- ZIENKIEWICZ, O. C., AND TAYLOR, R. L. 1989 *The Finite Element Method*, McGraw Hill.
- VAN ZUIJLEN, A. H., DE BOER, A., AND BIJL, A. 2007 Higher-order time integration through smooth mesh deformation for 3D fluid-structure interaction simulations, *Journal of Computational Physics*, **224**, 414–430.

## Bibliography

- BECKERT, A. 2000 Coupling fluid (CFD) and structural (FE) models using finite interpolation elements, *Aerospace Science and Technology*, **4**, 1, 13–22.
- CASADEI, F., HALLEUX, J. P., SALA, A., AND CHILLE, F. 2001 Transient fluid structure interaction algorithm for large industrial applications, *Computer Methods in Applied Mechanics and Engineering*, **190**, 3081–3110.
- SO, R. M. C., LIU, Y., AND LAI, Y. G. 2002 Mesh shape preservation for flow-induced vibrations problems, *Proceedings, International Mechanical Engineering Congress and Exposition*, 17–22 November, New Orleans, LA.